ACS Catalysis

pubs.acs.org/acscatalysis Research Article

Dynamic Features of Cu-Ceria Interface under CO_2 Hydrogenation to Methanol

Yuanyuan Li,* Yiming Chen, Haohong Song, Kinga A. Unocic, Jorge Perez-Aguilar, Jiyun Hong, Adam S. Hoffman, Jorge Moncada, Jeongjin Kim, Luke Daemen, Yongqiang Cheng, Caiqi Wang, Sanjaya D. Senanayake, Simon R. Bare, De-en Jiang, and Zili Wu

Cite This: *ACS Catal.* 2026, 16, 1132−1143 Read Online

ACCESS | Metrics & More | Article Recommendations | Supporting Information

ABSTRACT: It is generally accepted that metal−support interaction is very important for the hydrogenation of CO_2 to methanol, but little has been revealed about the feature of interfacial active sites under real reaction conditions since there are only limited techniques that can be applied under high-pressure conditions. In this work, by combining multiple in situ and operando techniques on a model Cu/ceria catalyst, we have tracked Cu and ceria sites for methanol formation. Under the reaction condition, it is found that upon reaching the reaction temperature, oxidized Cu species in the as-synthesized catalyst immediately change into metallic Cu species. Following this, it is the gradual formation of methanol, the changing rate of which coincides with the formation of a unique Ce^{3+} species. The combined experimental results and density functional theory (DFT) calculations have determined that the formed Ce^{3+} sites driven by the reaction conditions are bound to hydrides, adsorbed carbonate species, and interfacial active Cu sites. The Cu-ceria interaction in this complex moiety is weak and can be easily disturbed with reaction environment variations, leading to dynamic changes at the interface upon the hydrogenation of active carbonate intermediates, which are precursors for the formation of methanol. The formation of this unique Cu−Ce^{3+} interface and its dynamicity lead to an increase of methanol selectivity from less than 20% to 60%. These results suggest that reactant-derived species (H^- and carbonate in this work) can be essential components of the active center with the functions of manipulating the metal−oxide interaction and directing reaction pathways.

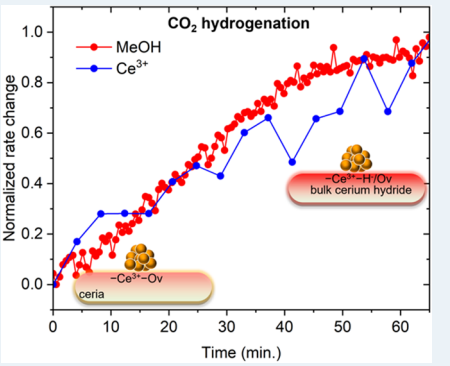

KEYWORDS: *CO_2 hydrogenation to methanol, operando studies, Cu/ceria, cerium hydride, carbonate intermediates, neutron scattering, high energy resolution fluorescence detected X-ray absorption*

INTRODUCTION

The reaction of CO_2 hydrogenation has been studied for decades due to its importance in producing valuable chemicals yet has presented challenges in determining and designing highly selective sites for the necessary high-pressure catalytic conditions. Taking CO_2 hydrogenation to methanol as an example, in industry, the produced methanol can be used as a fuel or to produce many other chemicals (such as formaldehyde, acetic acid, and plastics). However, in practice, along with this reaction is the competing reverse water gas shift reaction, which leads to the formation of the primary byproduct, CO. As a result, currently, there are few systems that show high methanol selectivity and yield in CO_2 hydrogenation, as summarized in several recent reviews.[1,2]

To improve the selectivity of methanol, many efforts have been made to reveal the nature of the active sites for methanol synthesis from CO_2 hydrogenation. Among those, however, there are limited studies focusing on working catalysts under the realistic high-pressure reaction condition. Consequently, the obtained information is usually ambiguous, and there are even intense debates about the active structure/phase such as in the commercial methanol synthesis catalyst $Cu/ZnO/Al_2O_3$ (CZA). For instance, Kattel et al. found that ZnCu became as active as ZnO/Cu only after it undergoes surface oxidation to form ZnO.[3] However, based on the XAS data of the $Cu/ZnO/Al_2O_3$ catalyst, Zabilskiy et al. found that Zn existed in two species (ZnO and CuZn alloy) in H_2 condition (15 bar and 533 K) and upon switching to CO_2 hydrogenation, a new Zn formate species showed up.[4] Regarding Cu, the reported active phase/site includes monometallic Cu, CuZn alloy, Cu surface defects, or Cu^{1+} ions.[5−7]

Although contradicting, these previous results, together with many other studies, pointed out the importance of Cu-oxide interface for methanol synthesis.[8−13] Inspired by these, we

Received: September 9, 2025
Revised: December 15, 2025
Accepted: December 16, 2025
Published: December 23, 2025

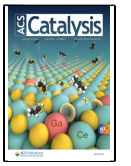

https://doi.org/10.1021/acscatal.5c06321
ACS Catal. 2026, 16, 1132−1143

recently engineered Cu/$BaTiO_3$ by introducing hydride anions into the support, and by doing so, the methanol selectivity and yield were significantly improved, suggesting that supports do have strong effects on activity and selectivity.[14] However, in that work, we did not observe support effects on the structure of Cu nanoparticle under the reaction condition.[14] In fact, in most of the previous reports, changes were not observed on Cu. As a result, there is no/little discussion on the nature of active sites at the Cu-support interface.[15] These results from our and other groups have puzzled us: *is it because the size of Cu species becomes too large under high-pressure CO_2 hydrogenation that most in situ/operando average techniques cannot detect the subtle change of active sites*? *Or are there other reasons that are unexpected or beyond intuition*?

Driven by these questions, we aim to provide detailed information about what is happening at the metal−support interface under the reaction conditions for the CO_2 hydrogenation. To achieve this goal, we will need to address the challenges associated with high-pressure conditions. First, many techniques that are crucial for surface or catalysis studies, such as electron-based imaging microscopy (transmission electron microscopy or scanning transmission electron microscopy−TEM/STEM) and soft X-ray-based spectroscopy (such as X-ray photoelectron spectroscopy−XPS), currently cannot be adapted to high-pressure measurements. Second, Infrared (IR) spectroscopy can be used to detect surface intermediates and surface metal species/sites with the presence of probe CO molecules. For CO_2 hydrogenation to methanol over Cu-based catalysts, the primary byproduct is CO under typical reaction temperatures (≤300 °C), and by taking advantage of it, in principle, the information about surface metal species/sites can be obtained under reaction conditions. However, under high-pressure CO_2 hydrogenation, the signals of gas-phase CO_2 dominate and even show bands in the characteristic range of adsorbed CO on metal sites, making it difficult to reveal the surface metal sites under reaction conditions.[16] Third, hard X-ray-based techniques, especially X-ray absorption spectroscopy (XAS), are the primary techniques that have been used in several studies to investigate the structure of catalysts under high-pressure reaction conditions.[4,17−20] The drawback of XAS is that it provides global average results. To detect changes, the sensitivity to the change of minority sites should be improved. Fourth, many developed systems for CO_2 hydrogenation to methanol are quite complex: for instance, Cu/ZnO/Al_2O_3, which is used in industry for methanol synthesis from syngas, is considered as a benchmark for CO_2 hydrogenation to methanol, but its structure involves multiple interfaces and sites, making it difficult to identify the information only from active sites.

To address the above-mentioned challenges, in this work, we apply in situ/operando techniques including XAS, neutron scattering, and IR spectroscopy on a simplified model system, Cu/ceria, to correlate its structural evolution with the time-dependent methanol selectivity and yield during CO_2 hydrogenation. The Cu/ceria system shows comparable performance with that of commercial Cu/ZnO/Al_2O_3.[8] In this study, under the similar testing condition, the methanol selectivity and yield over Cu/ceria are 60% and 160 mg/h/g_{Cu}, respectively (Figure S1), while for commercial Cu/ZnO/Al_2O_3, they are 48% and 230 mg/h/g_{Cu}.[14] To improve the sensitivity of XAS, we combine conventional and high energy resolution fluorescence detected (HERFD)−XAS. To detect the surface Cu sites by using IR, we keep the spent catalyst (spent means the catalyst has been exposed to the reaction condition) sealed and perform CO probed diffuse reflectance infrared Fourier transformed spectroscopy (DRIFTS). For techniques that cannot be used under high-pressure conditions (such as ambient pressure (AP) XPS and TEM), we mimic reactive conditions to provide complementary information about the active sites. By applying these strategies and with the assistance of DFT calculations and simulations, the nature of the interfacial active center for the formation of methanol and its dynamic change under the reaction are compellingly revealed.

EXPERIMENTAL SECTION

Sample Preparation. The Cu/ceria sample was prepared by dispersing 2.49 g cerium(IV) oxide nanopowder (<25 nm) in a solution of 3.0 g urea and 25 mL of water. The desired amount (5.01 mL) of Cu precursor solution (Copper(II) nitrate trihydrate in water, approximately 2.6 wt % Cu) was then added. The mixture was sealed in a round-bottom flask and stirred for 24 h in an oil bath at 95 °C. Following this deposition process, the samples were separated and washed by 3 cycles of centrifuging/redispersing in DI water to remove the residual ions from precursors. After drying overnight in an oven at 80 °C, the samples were crushed into powders and calcined at 500 °C for 5 h. The resulting Cu loading of the sample was measured by Inductively Coupled Plasma (ICP) elemental analysis and determined to be 3.2 wt %.

Catalytic Performance Tests. For the catalytic performance test, about 0.2 g of catalyst mixed with 1.0 g of quartz sand was loaded into the reactor (PID Eng & Tech) and a mixture of gas composed of 72% H_2, 24% CO_2, and 4% Ar was introduced at a flow rate of 15.5 mL/min. The catalytic performance was tested at 220 °C and 30 bar. An online gas chromatograph (Agilent) equipped with a flame ionization detector (FID) and a thermal conductivity detector (TCD) was used to analyze all products. A Porapak Q and a Carboxen column were utilized for separating the reactants and products.

D_2 Temperature-Programmed Reduction (TPR). About 100 mg of the used sample was loaded into a quartz reactor and pretreated under a He flow (30 mL/min) at 120 °C for 1 h. The pretreatment was to remove physiosorbed water. After pretreatment, the reactor was cooled to 50 °C, and the gas feed was switched to D_2 (30 mL/min) for purging for 1 h. The temperature was then increased from 50 to 500 °C at a heating rate of 10 °C/min. The effluent gas of HD from exchange between gas-phase D_2 and mostly the hydride (H^-) species in ceria was continuously monitored using a mass spectrometer (Pfeiffer Vacuum). For comparison, the fresh catalyst was pretreated and studied in the same manner to monitor the exchange between gas-phase D_2 and surface hydroxyls (OH).

Ambient Pressure X-ray Photoelectron Spectroscopy. Ambient pressure X-ray photoelectron spectroscopy (AP-XPS) studies were conducted using a SPECS chamber equipped with a PHOIBOS 150 EP MCD-9 analyzer (Chemistry Division, BNL) using a Mg Kα anode as X-ray source (energy resolution 0.4 eV, pass energy 30 eV).[21] XPS spectra were collected at UHV and 30 mTorr of H_2 using a 300 μm aperture cone and a differentially pumped analyzer electron optics for collection of electrons at elevated pressure while keeping the analyzer under near UHV.[22] Cu 2p and Ce 3d spectra were measured under reducing conditions at room temperature, 150, and 250 °C.

Neutron Scattering. The inelastic neutron scattering spectrum was collected at the VISION beamline. VISION is an inverted geometry spectrometer used for neutron vibra-

https://doi.org/10.1021/acscatal.5c06321
ACS Catal. 2026, 16, 1132−1143

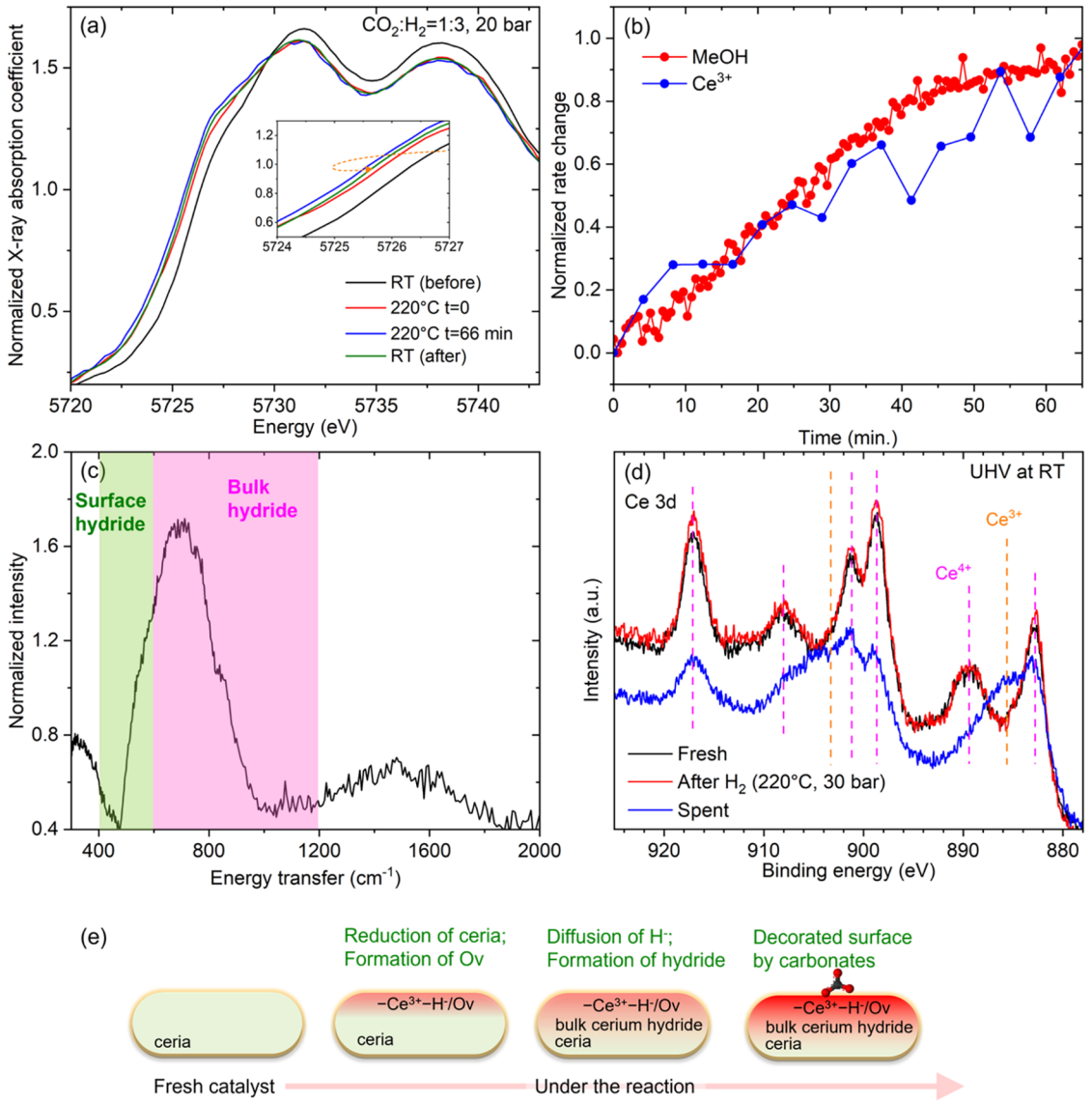

Figure 1. (a) Ce L_3 edge XANES spectra of Cu/ceria before (CO_2/H_2 = 1:3; 20 bar; RT), during (CO_2/H_2 = 1:3; 20 bar; 220 °C), and after (CO_2/H_2 = 1:3; 20 bar; RT) the reaction. (b) The normalized changing rate of methanol and Ce^{3+} species. (c) The in situ inelastic neutron scattering spectrum of the spent Cu/ceria. (d) The Ce 3d XPS spectra of the fresh, H_2-treated, and spent Cu/ceria catalyst. All catalysts were exposed to air for 4 months. (e) Changes of ceria under the reaction. Note, for a ceria hydride, hydrogen is H^-.

tional spectroscopy at the pulsed spallation neutron source (SNS) at Oak Ridge National Laboratory. VISION uses the time-of-flight technique to measure the energy of neutrons incident on the sample. The final neutron energy is set by the Bragg reflection on pyrolytic graphite analyzers. The dynamic range is 0 to ~6000 cm^{-1}. The energy resolution in that range is approximately 1 to 1.5%.[23] The sample was loaded in a stainless steel sample holder (19 mm diameter × 60 mm height) sealed with copper gaskets. A capillary tube connected to the sample holder allowed for the evacuation and gas loading. The sample was heated to 120 °C under vacuum for 1 h to remove any adsorbed water and gases. This sample was cooled to 5K at the VISION beamline, and a neutron vibrational spectrum was collected for 2 h to serve as background for the subsequent measurements. This sample was then warmed up to room temperature and exposed to a CO_2/H_2 gas mixture (1:3 molar ratio, 30 bar) at 220 °C for 3 h. The sample was then cooled to 120 °C, decreased to atmospheric pressure, and purged with helium for several minutes to remove physisorbed species. The sample was then cooled to 5 K, and a neutron vibrational spectrum was collected for 3 h.

In Situ STEM Measurement. In situ closed gas cell microscopy was conducted using an aberration-corrected JEOL 2200FS operated at 200 kV and the Protochips Atmosphere gas reaction system for the in situ STEM experiments. Protochips Atmosphere system allows us to perform study on a range of material systems in response to temperatures up to 1000 °C and pressures up to 1 atm (760 Torr) within a reactive gas environment to study the structural and chemical changes of Cu/ceria sample. Samples were drop cast on the silicon nitride window of a Protochips E-chip heater chip. The gas cell was flushed three times with nitrogen from 100 to 0.1 Torr to ensure there was no O_2 present in the system. The pressure was then set to 760 Torr, and the gas cell was filled with 100% H_2. Due to the geometry of the manifold

https://doi.org/10.1021/acscatal.5c06321
ACS Catal. 2026, 16, 1132−1143

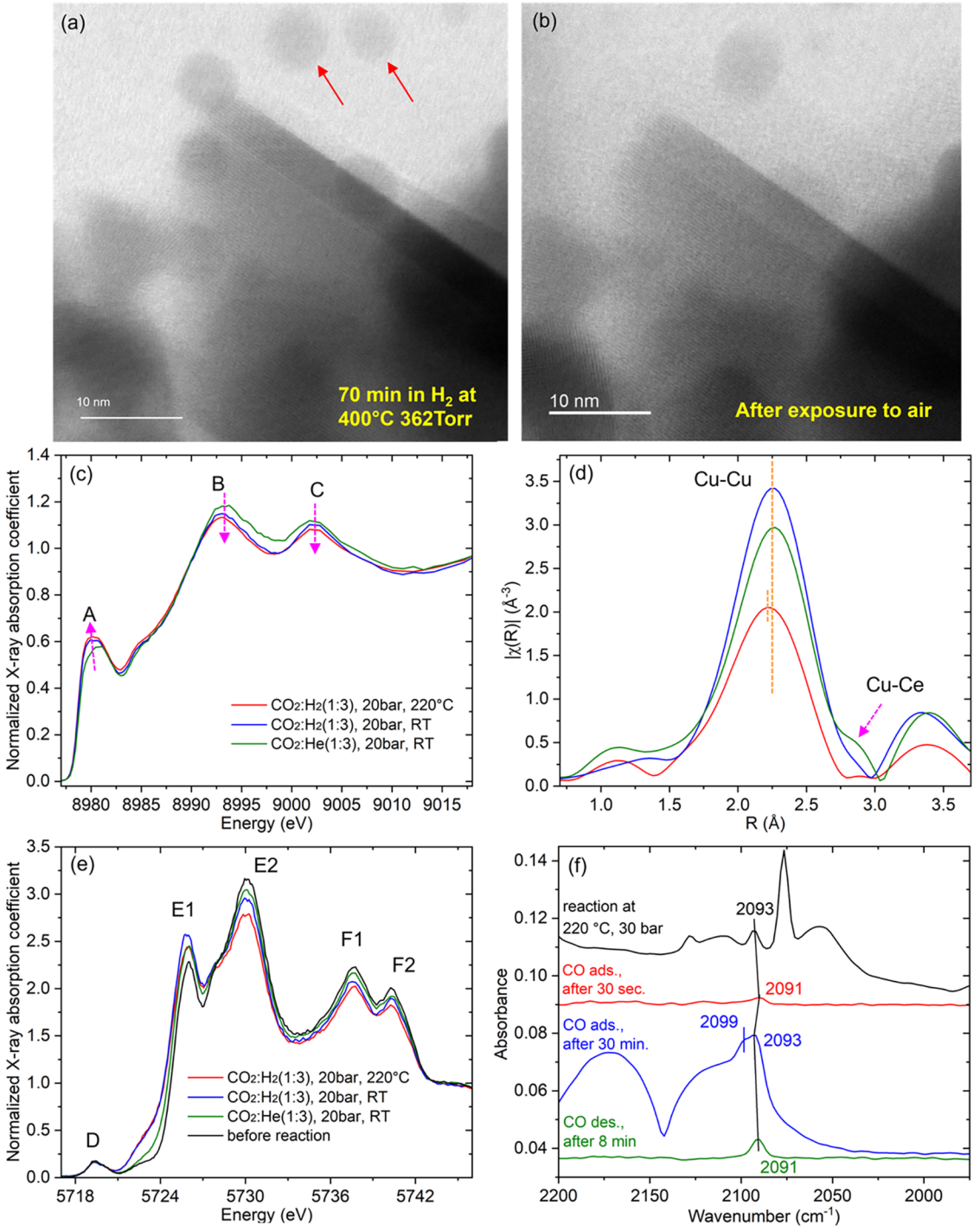

Figure 2. (a) Bright field (BF)-STEM image of Cu/ceria collected in H_2 at 400 °C and 362 Torr. The catalyst in (a) was subsequently exposed to air, and its BF-STEM image in (b) was taken after 2 days. (c) Cu K edge XANES and (d) EXAFS spectra of the spent Cu/ceria in different conditions and in HERFD mode. (c) and (d) share the same legend. (e) Ce L_3 edge HERFD−XANES spectra of the spent Cu/ceria collected in different conditions. (f) DRIFTS spectra of Cu/ceria under CO_2/H_2 (1:3)/20 bar/220 °C, CO (ambient pressure/RT) adsorption and after CO desorption.

that holds the supply gas tanks and continuous flow of the H_2 during the experiment, there was a pressure drop with time that was constantly reset. The temperature was brought from room temperature to 400 °C under flowing 100% H_2 at 5 °C/min. The exposure to the electron beam was minimized by blinking the beam exposure.

In Situ/Operando XAS Measurement. The Cu K edge and Ce L_3 edge conventional XAS spectra were collected at beamlines 4−3 and 9−3, and the HERFD-XAS spectra were collected at beamline 15−2 of the Stanford Synchrotron Radiation Lighthouse (SSRL) at SLAC National Accelerator Laboratory. The sample powder was loaded to a quartz capillary (0.98 mm I.D. and 0.02 mm wall thickness) reactor, which can hold pressure up to 20 bar.[24] The XAS data were collected in fluorescence mode. For the measurement of Ce L_3 edge XAS data, the sample powder was diluted with silica

https://doi.org/10.1021/acscatal.5c06321
ACS Catal. 2026, 16, 1132−1143

(1:10). For the data plotted in Figure 1, the as-prepared catalyst was exposed to the reaction conditions (CO_2/H_2 = 1:3; 20 bar). Subsequently, the reaction temperature was increased to 220 °C at a ramp rate of 10 °C/min. Once the temperature reached 220 °C, the time-dependent XAS spectra were collected. For the data plotted in Figure 2, the spectra were first collected under the reaction conditions (CO_2/H_2 = 1:3; 20 bar, 220 °C). Second, the reaction temperature was dropped to room temperature (CO_2/H_2 = 1:3; 20 bar, RT). Third, H_2 was replaced with He (CO_2/He = 1:3; 20 bar, RT). For reference, the spectra of the as-prepared catalyst were also collected.

DRIFTS Measurement. IR measurements were performed by using a Bruker FTIR spectrometer equipped with Praying Mantis High Temperature Reaction Chambers and an MCT detector. The as-synthesized catalyst, weighing approximately 60 mg, was loaded into the DRIFTS cell. Each spectrum was collected with 128 scans at a resolution of 4 cm^{-1}. For the switch experiments, under steady state reaction conditions (220 °C and 30 bar), the reactants (24%$^{12}CO_2$/72%H_2/4%Ar) were switched to 24%$^{13}CO_2$/72%H_2/4%He, Ar, or H_2. During the switch, the IR spectra were collected continuously to follow any spectral changes. For the CO−DRIFTS experiment, after the reaction condition (24%CO_2/72%H_2/4%Ar reaction at 220 °C and 30 bar), the reactants were flushed away by He, the temperature was dropped to RT, the pressure was decreased to ambient pressure, and subsequently, CO was introduced to detect the surface accessible Cu sites. When the spectra reached a steady state, CO was flushed away by He to check the reversibility. During CO adsorption and desorption, the IR spectra were collected continuously.

CO Pulse Adsorption Experiment. The CO pulse adsorption experiment was conducted by using an AMI-300 Chemisorption Analyzer (Altamira Instruments). Approximately 200 mg of the used catalyst was loaded into a quartz reactor. Three types of pulse experiments were performed. First, the spent catalyst was pretreated under a He flow (20 mL/min) at 120 °C for 1 h to remove physically adsorbed species and water. After pretreatment, the reactor was cooled to 50 °C and maintained under a He flow (20 mL/min). Pulses of 2 vol % CO/He were introduced into the reactor using a 0.514 mL injection loop. By doing this experiment, we can estimate the number of exposed copper sites from CO adsorption on the spent catalyst. Second, after 10 pulses of 2 vol % CO/He, the gas flow was switched to H_2, and the reactor was heated to 220 °C and held for 1 h. By doing this, we can remove some of the surface adsorbates. The reactor was then cooled to 50 °C, and the CO pulse sequence was repeated under the same conditions. By doing this experiment, we can estimate the CO adsorption on the spent catalyst with reactive surface species being removed. Third, the reactor was again pretreated in H_2 at 220 °C for 1 h, followed by cooling to 50 °C under He flow (20 mL/min). Ten pulses of CO_2 were then introduced into the reactor, followed by another 10 pulses of 2 vol % CO/He. By doing this, we can study the competitive adsorption of CO and CO_2. For all pulse experiments, the effluent gas was continuously monitored by a thermal conductivity detector (TCD).

DFT Computation. Density functional theory (DFT) calculations were performed using the Vienna Ab initio Simulation Package (VASP).[25,26] The Perdew−Burke−Ernzerhof (PBE) functional of generalized-gradient approximation (GGA) was employed for electron exchange and correlation.[27] The electron−core interaction was modeled using the projector-augmented wave method (PAW).[28,29] The vdW-DF functional[30] was used to improve the prediction of CO adsorption energies on the copper cluster.[31] The on-site Coulomb interaction was considered by employing the DFT + U method by Dudarev et al. with a U value of 4.5 eV for Ce 4f localized electrons based on previous studies.[32−34] Plane-wave kinetic energy cutoff was set to 500 eV to treat the valence electrons.

The bulk cerium oxyhydride with a composition of $CeO_{1.75}H_{0.25}$ was modeled by replacing one O atom in the Ce_4O_8 fluorite-structure unit cell with H; the optimized lattice parameter is 5.47 Å. Then, the (111) surface of $CeO_{1.75}H_{0.25}$ was created with three $CeO_{1.75}H_{0.25}$ sandwich layers and a vacuum layer of 15 Å in thickness. The bottom $CeO_{1.75}H_{0.25}$ sandwich layer was fixed during geometry optimization. The Brillouin zone of the surface slab was sampled using the Monkhorst−Pack scheme, with a (2 × 2 × 1) k-mesh. Next, a Cu_{12} cluster was placed on the surface, followed by a carbonate species from CO_2 adsorption and reaction with a surface O site. The adsorption energy is calculated by

$$E_{ads} = E_{slab/CO} - E_{slab} - E_{CO}$$

where $E_{slab/CO}$ represents the system energy of slab with the adsorbed CO, and E_{slab} and E_{CO} represent the energies of the clean slab and the gas-phase CO in a large box, respectively. A scaling factor of 1.03 based on the gas-phase CO vibrational frequency was used to calibrate the adsorbed CO frequency. The equilibrium structures were optimized with a force convergence criterion of 0.01 eV/Å. The vibrational frequencies were computed using the finite-difference method with a displacement of 0.02 Å for the C and O atoms only. Dipole corrections were included. Frequency calculations were performed using both the PBE + U and HSE06 functionals to assess the influence of electron exchange−correlation on the computed vibrational frequencies.

RESULTS AND DISCUSSION

Correlated Formation of Methanol and Ce^{3+} Hydride. The time-resolved Cu K edge and Ce L_3 edge XAS spectra under the reaction condition (CO_2/H_2 = 1:3; 20 bar; 220 °C) are collected to track the change of Cu/ceria catalyst. As shown in Figure S2, upon heating the Cu/ceria catalyst under the reaction environment at 20 bar from RT to 220 °C, oxidized Cu species is readily reduced to Cu metal. Thereafter, there are no time-dependent changes of Cu K edge spectra at 220 °C. Based on the EXAFS data analysis (Figure S3 and Table S1), during the reaction, the average coordination number (CN) of Cu−Cu is 10.8 ± 0.3, smaller than that in Cu foil (12); the average bond distance of Cu−Cu is 2.534 ± 0.002 Å, shorter than that in Cu foil (2.542 ± 0.002 Å), suggesting the formation of nanosized Cu nanoparticles under the reaction condition. The estimated average particle size of Cu nanoparticles is ∼4.5 nm under the high-pressure reaction condition.[35] This changing trend of Cu is similar to those previously observed in other Cu-based systems.[4,14,17]

Interestingly, a time-dependent change is observed from Ce L_3 edge XANES spectra (Figures 1a and S4). There is an increase in the concentration of Ce^{3+} at longer reaction time, as evidenced by the increased shoulder peak at about 5727 eV.[36−38] Cooling the sample to room temperature causes the reversed shift of the Ce L_3 edge. Linear combination fitting is performed on the time-resolved XANES spectra (Figure S4).

https://doi.org/10.1021/acscatal.5c06321
ACS Catal. 2026, 16, 1132−1143

The increasing rate of Ce^{3+} is similar to that of methanol (Figure 1b), detected by using an online Hiden mass spectrometer (Figure S5). The coincident change of Ce^{3+} and methanol selectivity/yield indicates a crucial role of oxide supports in determining the methanol selectivity and a transformation of some ceria sites from CO-selective to methanol-selective. Since ceria itself is barely active under the same reaction conditions, these developed Ce^{3+} sites must interact with interfacial Cu sites.

The in situ inelastic neutron scatting spectrum (Figure 1c) collected over the Cu/CeO_2 catalyst after being exposed to the reaction condition for 3 h (CO_2/H_2 = 1:3; 30 bar; 220 °C) shows the existence of surface and bulk Ce hydrides (in which hydrogen is H^-) in the spent Cu/ceria, as evidenced by the pronounced peak ranging from 500 to 1000 cm^{-1}.[39] Based on D_2 TPR experiments (Figure S6), the ratio between the surface and bulk hydrides is about 0.3 and surface hydrides likely play a larger role than bulk ones in CO_2 hydrogenation due to their higher reactivity under the reaction temperature. The generated surface hydrides are likely covered and protected by CO_2-derived species under CO_2 hydrogenation conditions. This is supported by our XPS study. Specifically, Figure 1d displays the Ce 3d XPS of fresh, H_2-treated (at 220 °C and 30 bar), and spent Cu/ceria catalysts. All three catalysts have been purposely exposed to air for an extended period (~4 months). As shown in Figure 1d, the spectra of fresh and H_2-treated samples are similar, and both are dominated by Ce^{4+} species (~93%), suggesting that the formed Ce hydride species under H_2-only condition at 220 °C and 30 bar is not stable after being exposed to air, due to the facile reaction between hydrides and O_2 at room temperature.[39] On the other hand, compared with the fresh and H_2-treated catalysts, the concentration of Ce^{3+} in the spent catalyst is still high (30.72%; Figure S7 and Table S2), suggesting that the stable Ce^{3+} species observed in the spent catalyst must also coexist with and thus be protected by surface species derived from the reaction, for instance, surface carbonates.

If that is the case, those carbonate species, in principle, can be removed by heating the spent catalyst in H_2 at elevated temperatures which should also lead to the recovery of Ce^{4+} species due to the regeneration of lattice oxygen atoms via reactions such as $CO_3^{2-} + H_2 \rightarrow CO/CH_3OH/H_2O/CO_2 + O_L$ (O_L stands for lattice oxygen). As expected, as shown in Figure S8a, by heating the spent catalyst in H_2 at elevated temperatures, the concentration of Ce^{3+} (Ce^{4+}) of the spent catalyst continues to decrease (increase). Such a trend is different from that observed for the H_2-treated Cu/CeO_2 catalysts. Specifically, for the H_2-treated catalyst (Figure S8b and Table S2), increasing the temperature in H_2 results in a decrease of the concentration of Ce^{4+} from RT to 250 °C. These contrasting observations, again, show the uniqueness of the ceria surface of the spent catalyst and suggest that under the reaction of CO_2 hydrogenation, the selective surface Ce^{3+} species could be associated with surface species like carbonates, implying that some carbonate species could be active reaction intermediates for methanol formation over Cu/ceria, as demonstrated in the IR study (discussed in the later section).

Based on these results, a schematic is proposed to show the change of ceria support under the reaction conditions (Figure 1e). When the reaction is occuring and at the initial stage of the reaction, the highly reducing environment and the fast formation of metallic Cu facilitate the formation of Ce^{3+} and oxygen vacancy (Ov). At those surface Ce^{3+}-Ov pairs, adsorbed CO_2 could be converted to CO, facilitated by the nearby Cu sites, via the redox reaction mechanism. Correspondingly, the high selectivity of CO (low selectivity of methanol) is observed at t = 0 min (Figures S1 and S5). With the progression of the reaction (the induction period), cerium hydride species are formed and detected. Along with the formation of hydride is the evolution of carbonates on the surface of ceria, until a steady state is achieved. Those carbonates decorate and stabilize surface Ce^{3+} sites, together with diffused H^-, leading to a unique ceria surface interacting with Cu nanoparticles that result in high selectivity to methanol (Figure S1). Under the reaction condition, the subtle change of ZnO in Cu/ZnO was also observed by Zabilskiy et al. due to the formation of Zn formate.[4]

These changes observed from ceria led us to address the following questions: Since Cu sits on the surface of ceria and the particle size of Cu is smaller than ceria, *why is the time-dependent change not observed in Cu and how does Cu interact with ceria under the reaction condition*? The next sections are organized to answer these questions.

Cu Sites and Dynamic Cu-Ceria Interaction at the Interface. For the above-mentioned question related to Cu, our hypothesis is that the interfacial interaction between ceria and Cu nanoparticles is weak and very dynamic under the highly reducing reaction conditions such that any change of Cu sites can be easily overlooked.

To test this hypothesis, in situ STEM measurements are performed over the Cu/ceria system. As shown in Figure 2a, Cu nanoparticles (~5 nm) which cannot be observed in the as-prepared catalyst (Figure S9) appeared in H_2 at 400 °C. The spherical shape of Cu nanoparticles, different from the typically observed truncated cuboctahedral shapes,[40] suggests their weak interaction with ceria support under reducing conditions. In addition, it appears that some Cu nanoparticles (labeled by red arrows) are not intimately contacting with ceria support (more figures in Figure S10). All of these indicate that Cu nanoparticles tend to separate from the ceria support in a highly reducing environment at elevated temperatures. The high mobility of these formed Cu nanoparticles is also evidenced by replacing the reactive condition from highly reducing to oxidizing. As shown in Figure 2b, being subsequently exposed to air, many Cu particles seen in Figure 2a (image taken from the same area) disappear and Cu nanoparticles are redispersed on the surface of ceria with time (Figure S9). Agreeing with these observations obtained from in situ STEM, the estimated average particle size of Cu nanoparticles is ~4.5 nm under the high-pressure reaction condition (based on the Cu−Cu coordination number obtained from EXAFS analysis; Table S1),[35] and exposing the spent catalyst to air leads to the oxidation and redispersion of Cu nanoparticles, as suggested by the XAS data (Figure S11). Such an agreement validates the information provided by the in situ STEM that under the reaction conditions, the interaction between Cu and ceria support is weak. Beyond this, the phenomenon of Cu detaching from ceria support under the reducing condition and reanchoring on the surface of ceria under the oxidizing condition implies that under the reaction condition, the coexistence of H_2 (reducing) and CO_2 (oxidizing) and their adsorption and conversion could lead to dynamic changes at Cu-ceria interface.

To detect the dynamic change of Cu and ceria, high energy resolution fluorescence detected (HERFD) XAS spectra are collected by exposing the catalyst to different reactive

https://doi.org/10.1021/acscatal.5c06321
ACS Catal. 2026, 16, 1132−1143

conditions. Compared with conventional XAS, HERFD−XAS spectra show a higher energy resolution, which helps the detection of responses from active sites that are in the minority.[41−47] Figure 2c displays the Cu K edge spectra of Cu/ceria, where three peaks, labeled as A, B, and C, are present in all spectra. Changing the condition from CO_2/He (1:3)/20 bar/RT to CO_2/H_2 (1:3)/20 bar/RT and to CO_2/H_2 (1:3)/20 bar/220 °C, the intensity of A gradually increases and those of B and C decrease, suggesting that (1) a small portion of Cu sites responds to the change of external conditions; (2) those responsive Cu sites tend to gain electrons in H_2 rich conditions and at elevated temperatures.

Along with the change in the local electronic structure of some Cu sites, their local atomic structure changes are also detected under different conditions. Figure 2d exhibits the corresponding R-space EXAFS spectra collected under conditions listed in Figure 2a. The k-space EXAFS spectra are shown in Figure S12. All R-space EXAFS spectra show a pronounced Cu−Cu metallic bond at ∼2.3 Å. In the CO_2/He (1:3)/20 bar/RT condition, an additional contribution at ∼2.8 Å can be observed. This contribution fades after the introduction of H_2 at RT and cannot be detected in the reaction condition (CO_2/H_2 (1:3)/20 bar/220 °C). Based on the EXAFS analysis (Figure S13 and Table S1), it is determined that the peak at ∼2.8 Å is due to Cu−Ce contribution. In CO_2/He (1:3)/20 bar/RT, the coordination number of Cu−Cu is 9.9 ± 0.7, smaller than that in the reaction condition (CO_2/H_2 (1:3)/20 bar/220 °C; CN = 10.8 ± 0.3). In the reaction condition (CO_2/H_2 (1:3)/20 bar/220 °C), the obtained Cu−Cu bond distance (2.528 ± 0.006 Å) is smaller than that in nonreaction conditions (∼2.545 Å). These results suggest that CO_2 tends to anchor Cu nanoparticles to ceria while the introduced H_2 tends to break the Cu-ceria interaction and along with it are the restructuring of Cu local structures (increased Cu−Cu coordination number and shortened Cu−Cu bond distance) and gaining of electrons (Figure 2a) of interfacial Cu sites.

A similar trend is observed in the Ce L_3 edge HERFD-XANES spectra, as shown in Figure 2e. All spectra display five prominent features labeled as D, E1, E2, F1, and F2.[42] Note S1 provides detailed peak assignments and discussion. Compared with the fresh catalyst, regardless of the gas conditions, the spectra of the spent catalyst show higher intensity of E1, lower intensity of E2, F1, and F2, and the appearance of features within 5721−5724 eV indicates a higher ratio of Ce^{3+} species in the spent catalyst (agreeing with results from Figure 1a,d). Compared with other gas conditions, CO_2 (CO_2/He (1:3)/20 bar/RT) tends to oxidize a certain amount of Ce^{3+} sites. Even at RT, the introduction of H_2 (CO_2/H_2 (1:3)/20 bar/RT) can weaken the effect of CO_2 on ceria, as evidenced by the increased E1 and decreased E2, F1, and F2. By elevating the temperature (CO_2/H_2 (1:3)/20 bar/220 °C), all peaks including E1, E2, F1, and F2 showed decreased intensity compared with those at RT (CO_2/H_2 (1:3)/20 bar/RT), due to a decrease in the density of unoccupied states of Ce which is associated with decreased ionic character, higher configurational disorder, smaller coordination number of neighbors, and/or weaker interaction with surface adsorbates.[48−50] As a result, under CO_2/H_2 (1:3)/20 bar/220 °C, the ceria surface interacts weakly with Cu, which also has a higher density of occupied states under the reaction (Figure 2c).

The HERFD−XAS results show that the physical and electronic interactions between Cu and ceria are aggressively manipulated by reactants under high-pressure conditions. Under the reaction conditions, Cu-ceria interaction is not only weak but also dynamic, which explains the unobserved time-dependent change of Cu.

To reveal the nature of active and selective Cu sites associated with Cu nanoparticles, a DRIFTS experiment is performed. We initially intended to analyze the IR spectra collected under the reaction condition. However, as mentioned earlier in the Introduction, some bands associated with gas-phase CO_2 overlap with those associated with Cu sites. Specifically, as shown in Figures 2f and S14, under the reaction condition (CO_2/H_2 (1:3)/30 bar/220 °C), the bands associated with gas-phase CO_2 dominate. Particularly, in the wavenumber range of 2200−1900 cm^{-1}, where bands due to CO on the surface Cu sites would show up, all the observed bands could also be associated with gas-phase CO_2, making it difficult to reveal surface Cu sites under the reaction condition.[16] To detect surface Cu sites, we therefore switched the feeding of CO_2 and H_2 during the reaction to He in the IR reactor to flush away other gases and remove some active intermediates as well as adsorbed CO so that the associated active Cu sites for methanol and CO formation could be revealed. After dropping the temperature and pressure to RT and ambient pressure, the sample is exposed to gas molecule CO, and time-resolved DRIFTS spectra are collected during the CO adsorption process (Figure S15a). To check the reversibility, subsequently, CO is replaced with He and time-resolved DRIFTS spectra during the CO desorption process are also recorded (Figure S15a).

As shown in Figure 2f, after 30 s of CO adsorption, a small band at 2091 cm^{-1} appears. With prolonged exposure time under CO, this band shifts slightly to 2093 cm^{-1} due to higher CO coverage.[51] In addition, a new band appears at 2099 cm^{-1}, suggesting that there are at least two types of accessible Cu sites on the surface. These two sites have different electronic or geometric structures and thus lead to different bonding properties with adsorbates such as CO. Specifically, although both 2093 and 2099 cm^{-1} bands are assigned to linearly bonded CO molecules on the surface of metallic Cu sites,[52,53] compared with the 2099 cm^{-1} band, the Cu site associated with 2093 cm^{-1} band has a stronger interaction with CO (based on the observation that it appears first in the CO adsorption process and remains after the desorption of 2099 cm^{-1} band in the CO desorption process; Figure S15a) due to a stronger back-donation of electron density from the Cu to CO, suggesting that the Cu site responsible for the 2093 cm^{-1} band has relatively higher electron density.[54] Furthermore, the low intensity of these bands (compared to the gas-phase CO bands and the case of CO adsorption over a fairly clean Cu/ceria surface in Figure S15b and Note S2) suggests the low concentration of the two types of accessible Cu sites, agreeing with HERFD−XAS result that there is only a small portion of Cu sites responding to the change of external conditions. These two types of accessible Cu sites are likely to be involved in CO_2 hydrogenation.

To provide more information about these two Cu sites, DFT calculations are performed to model the Cu/ceria interface as well as CO adsorption at the interface. Based on the experimental findings, we construct a bulk cerium oxyhydride with a composition of $CeO_{1.75}H_{0.25}$; namely, 1/8 of O^{2-} anions are replaced with hydrides and the average oxidate state of Ce is now +3.75 due to 3/4 Ce^{4+} and 1/4 Ce^{3+}. Then, we create the (111) surface from the bulk $CeO_{1.75}H_{0.25}$ and one can see

https://doi.org/10.1021/acscatal.5c06321
ACS Catal. 2026, 16, 1132−1143

the surface hydrides on the support (Figure 3a). A more detailed analysis of Ce oxidation states was also performed by computing the Bader charges (Figures S16 and S17, and Table S3). Next, we place a Cu nanoparticle modeled by a hemispherical Cu_{12} nanocluster on the surface[55] and optimize the structure (Figure 3b): the interaction between the Cu nanoparticle and the $CeO_{1.75}H_{0.25}$ surface features strong Cu−H bonds of relatively short distances at 1.58 Å, which have been observed in copper-hydride nanoclusters and complexes.[56,57] We note that the Cu_{12} cluster that we used to model Cu nanoparticles is much smaller than the ∼4.5 nm Cu nanoparticles observed experimentally. Addressing this material gap would be very computationally demanding but could further address the transferability of the conclusions based on the smaller model regarding interfacial charge transfer, CO frequencies, and role of hydrides. A follow-up computational study of larger sizes and different shapes and morphologies is warranted. To simulate the carbonate species, we allow a CO_2 molecule to react with a surface O site and form a surface carbonate; we test different O sites and found the most stable one being at the interface where one of the carbonate O atoms directly bonds with an interface Cu atom (Figure S18). Pristine $CeO_{1.75}H_{0.25}$ surface has 6 out of 16 Ce sites that have oxidation states close to 3+. After Cu_{12} cluster adsorption, the number of such sites increases from 6 to 8, and further to 9 following interfacial carbonate adsorption. This gradual increase indicates that both the Cu cluster and the CO_3 species promote reduction of Ce^{4+} on the surface. Based on the $Cu_{12}/CeO_{1.75}H_{0.25}$-carbonate model, we then explore different CO adsorption sites. We find that the most stable site for CO is on top of an interfacial Cu atom that is bonded to a surface hydride (CO configuration 1; Figure 3c), and the calculated CO vibrational frequency of 2093 cm^{-1} closely matches that of the experiment. The next stable interfacial site for CO adsorption (CO configuration 2; Figure 3d) is on top of a Cu site next to the hydridic Cu and the calculated CO vibrational frequency of 2098 cm^{-1} also agrees well with the experiment (2099 cm^{-1}). To clarify the influence of interfacial carbonate species, we also performed calculations for the adsorption of CO on $Cu_{12}/CeO_{1.75}H_{0.25}$ and compared with $Cu_{12}/CeO_{1.75}H_{0.25}$-carbonate (Table S4). Based on the results obtained on the Bader charges of different Cu sites (Tables S5 and S6, and Figure S19), the hydridic Cu site is relatively electron-rich compared with the site next to it.

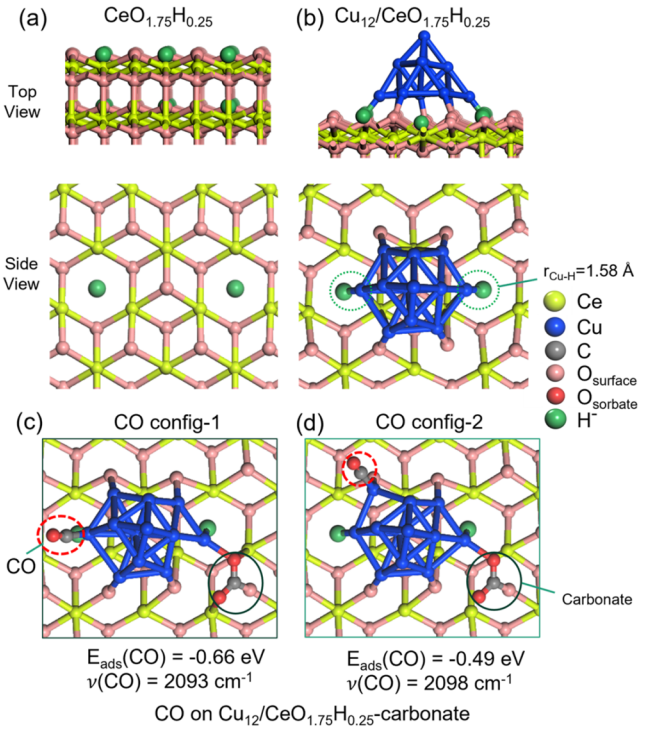

Figure 3. DFT modeling of CO adsorption on $Cu_{12}/CeO_{1.75}H_{0.25}$-carbonate: (a) the (111) surface of $CeO_{1.75}H_{0.25}$; (b) the Cu_{12} nanocluster supported on the (111) surface of $CeO_{1.75}H_{0.25}$; (c) the most stable configuration of interfacial CO adsorption on $Cu_{12}/CeO_{1.75}H_{0.25}$-carbonate (CO config-1); (d) the next most stable configuration of interfacial CO adsorption on $Cu_{12}/CeO_{1.75}H_{0.25}$-carbonate (CO config-2).

Active Reaction Intermediates and Reaction Mechanisms. To determine the nature of active reaction intermediates, the intermediates over the Cu/ceria system under the reaction of CO_2 hydrogenation are monitored by performing an isotopic switch experiment under steady state

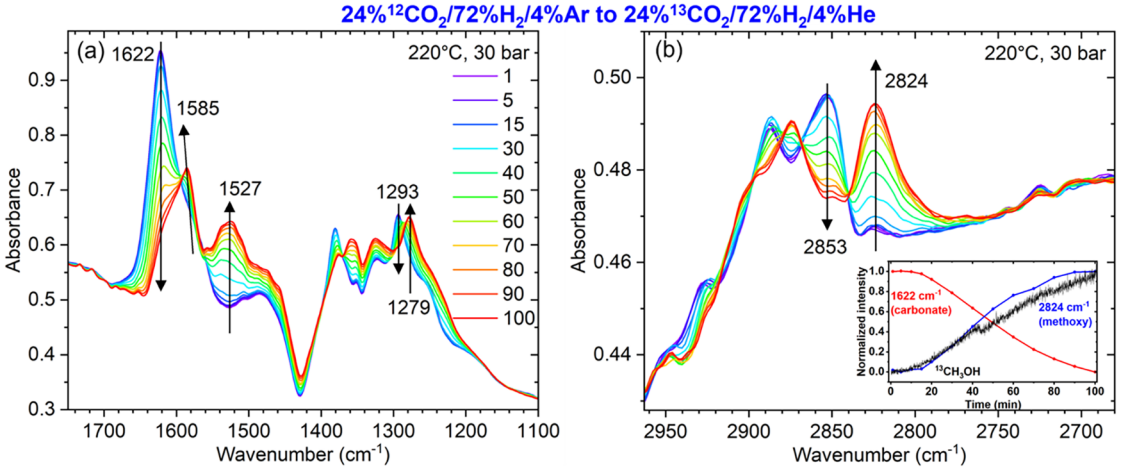

Figure 4. DRIFTS spectra collected at 220 °C and 30 bar upon the switch of the gas environment from 24%$^{12}CO_2$/72%H_2/4%Ar to 24%$^{13}CO_2$/72%H_2/4%He. (a) and (b) share the same legend. The inset in (b) shows the changing rate of the bands at 1622 and 2824 cm^{-1} and $^{13}CH_3OH$ (detected by using a mass spectrometer) after the ^{12}C-to-^{13}C exchange.

https://doi.org/10.1021/acscatal.5c06321
ACS Catal. 2026, 16, 1132−1143

condition (switching of the reactant from H_2+ $^{12}CO_2$ to H_2+ $^{13}CO_2$) and collecting IR spectra during the process. As shown in Figure 4, multiple IR bands exist under the reaction condition and generally, they are assigned to carbonate, formate, or methoxy species (Table S7).[14,58−65] Upon $^{12}CO_2$-to-$^{13}CO_2$ exchange, along with the shift of the bands assigned to carbonate and formate species is the shift of the bands assigned to methoxy species (2853 cm^{-1} to 2824 cm^{-1}),[61−65] suggesting that both carbonate and formate species could be active intermediates for the formation of methanol over the Cu/ceria system. Despite this, in the C−O region (Figure 4a), the most significant change is observed from the band at 1622 cm^{-1}. This band, together with the one at 1293 cm^{-1}, is assigned to tridentate carbonate and its corresponding ^{13}C labeled species located at 1585 and 1279 cm^{-1}.[58] Note, after the switch, the weak intensity of the 1585 cm^{-1} band and the increased 1527 cm^{-1} band suggest that the 1585 cm^{-1} band is also associated with other types of carbonate species or formates.[14,58−60] By analyzing the intensity change of the bands at 1622 and 2824 cm^{-1} and the mass spectrum of $^{13}CH_3OH$ as a function of reaction time, it is found that the decay rate of the unlabeled tridentate carbonate species mirrors the formation rate of the labeled methoxy species and gas-phase methanol (Figure 4b inset), suggesting that some of the carbonates (not all types of carbonates) could be active reaction intermediates for methanol formation from CO_2 hydrogenation over Cu/ceria.[66−68] In addition, by monitoring the change of surface species after changing the condition from the reaction to either Ar or to H_2 (Figure S20), it is found that the carbonate species at 1622/1293 cm^{-1} are more readily responding to the change of gas environment than other species, highlighting the higher reactivity of the carbonate species. The DRIFTS spectra in Figure S20, together with those XPS data (Figure S7a), which show the removal of surface CO_2-derived species and the recovery of Ce^{4+} species in H_2 at elevated temperatures, suggest that those responding carbonate species are correlated with the selective surface Ce^{3+} hydride species created and increased during the reaction condition.

Based on the combined results, a schematic (Figure 5) is proposed to show the dynamic catalytic behavior of Cu/ceria for the reaction of the hydrogenation of CO_2 to methanol. Under the reaction, there are three types of surface Cu sites. For the first type, the golden ones in the schematic, they are in the majority but do not actively participate in the reaction due to their strong bonding with inactive reaction intermediates (as indicated by the low density of Cu sites accessible by CO probing in Figure 2f). For the second type, the green one in the schematic, they do not directly interact with the H^- site (Figure 3d) and have relatively weak interaction with CO (Figure 2f), which could result in facile CO desorption and contribute to CO selectivity. This assumption is supported by the catalytic behavior of Cu/ceria shown in Figure S1: at the early stage of the reaction when the hydride species are yet to be fully formed, the dominant product is CO. For the third one, the magenta Cu in the schematic, it is bonded to a surface hydride and can stabilize carbonate intermediates (Figure S18). It has unique electronic properties: compared with other interfacial Cu sites, it is relatively electron-rich; compared with other surface Cu sites (away from the interface), it is relatively electron-deficient (Table S5). When combined with the activity data and the change of ceria species (Figures 1 and S1), such local electronic and atomic features of the magenta Cu could be responsible for the selective CO_2 hydrogenation to methanol. These features could allow the creation of a dynamic interfacial zone with dominant control of the reactants. For the proceeding of the reaction, the interfacial active carbonate intermediate could be hydrogenated by cerium hydride or by the reactant H_2. For the former, an increase of methoxy species (Figure S21), along with the decrease of carbonate species (Figure S20a) is observed when replacing the reaction condition with Ar, implying an active role of hydrides in hydrogenating surface carbonate to methanol. More experimental and theoretical work will be performed to elaborate events that occurred at the accessible interfacial Cu sites, including the catalytic role of the lattice hydrides.

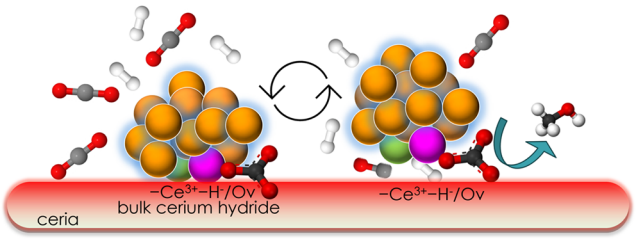

Figure 5. Schematic showing the catalytic behavior of Cu/ceria during the reaction. The magenta sphere represents the accessible hydridic Cu site, and the green sphere represents the accessible Cu site that does not directly interact with H^-.

CONCLUSION

This work focuses on revealing the feature of the Cu−ceria interface for the reaction of CO_2 hydrogenation to methanol by combining multiple in situ and operando techniques (including STEM, XAS, HERFD−XAS, AP-XPS, neutron scattering, and DRIFTS) and DFT calculations/simulations on a working Cu/ceria catalyst. The combined results show the correlated methanol formation with the increase in Ce^{3+} species. This unique Ce^{3+} species is formed due to the strong effects of reactants: the dissociated H_2 leads to the formation of bulk and surface cerium hydride, which is stabilized and protected by carbonate species. The intrusion and chemical bonding of these reactant-derived species at Cu-ceria interface modify and manipulate the Cu-ceria interaction under the reaction, with the proceeding of the reaction: the hydrogenation of active carbonates is associated with the dynamic change at Cu-ceria interface. With these insights, to form more of active interfacial site, one may consider the synthesis of Cu core−ceria shell structures and design ceria surfaces enriched with hydride structures and protective carbonate layers.

ASSOCIATED CONTENT

Supporting Information

The Supporting Information is available free of charge at https://pubs.acs.org/doi/10.1021/acscatal.5c06321.

Discussion of Ce L_3 edge HERFD-XANES spectra; catalytic performance; additional characterization data; XAS and XPS data analysis; DFT calculation structures; and calculated Bader charge of Ce and Cu sites (PDF)

https://doi.org/10.1021/acscatal.5c06321
ACS Catal. 2026, 16, 1132−1143

AUTHOR INFORMATION

Corresponding Author

Yuanyuan Li − *Chemical Sciences Division, Oak Ridge National Laboratory, Oak Ridge, Tennessee 37831, United States;* orcid.org/0000-0003-3074-9672; Email: liy4@ornl.gov

Authors

Yiming Chen − *Department of Chemical and Biomolecular Engineering and Department of Chemistry, Vanderbilt University, Nashville, Tennessee 37235, United States*

Haohong Song − *Department of Chemical and Biomolecular Engineering and Department of Chemistry, Vanderbilt University, Nashville, Tennessee 37235, United States;* orcid.org/0009-0003-2037-7905

Kinga A. Unocic − *Center for Nanophase Materials Sciences, Oak Ridge National Laboratory, Oak Ridge, Tennessee 37831, United States; Department of Materials Science and Engineering, North Carolina State University, Raleigh, North Carolina 27606, United States*

Jorge Perez-Aguilar − *Stanford Synchrotron Radiation Lightsource, SLAC National Accelerator Laboratory, Menlo Park, California 94025, United States;* orcid.org/0000-0001-8650-3132

Jiyun Hong − *Stanford Synchrotron Radiation Lightsource, SLAC National Accelerator Laboratory, Menlo Park, California 94025, United States;* orcid.org/0000-0002-3631-0559

Adam S. Hoffman − *Stanford Synchrotron Radiation Lightsource, SLAC National Accelerator Laboratory, Menlo Park, California 94025, United States*

Jorge Moncada − *Chemistry Division, Brookhaven National Laboratory, Upton, New York 11973, United States*

Jeongjin Kim − *Chemistry Division, Brookhaven National Laboratory, Upton, New York 11973, United States;* orcid.org/0000-0002-3790-1684

Luke Daemen − *Neutron Scattering Division, Oak Ridge National Laboratory, Oak Ridge, Tennessee 37831, United States*

Yongqiang Cheng − *Neutron Scattering Division, Oak Ridge National Laboratory, Oak Ridge, Tennessee 37831, United States;* orcid.org/0000-0002-3263-4812

Caiqi Wang − *Chemical Sciences Division, Oak Ridge National Laboratory, Oak Ridge, Tennessee 37831, United States;* orcid.org/0000-0001-9884-9990

Sanjaya D. Senanayake − *Chemistry Division, Brookhaven National Laboratory, Upton, New York 11973, United States;* orcid.org/0000-0003-3991-4232

Simon R. Bare − *Stanford Synchrotron Radiation Lightsource, SLAC National Accelerator Laboratory, Menlo Park, California 94025, United States;* orcid.org/0000-0002-4932-0342

De-en Jiang − *Department of Chemical and Biomolecular Engineering and Department of Chemistry, Vanderbilt University, Nashville, Tennessee 37235, United States; Department of Chemical and Biomolecular Engineering, Vanderbilt University, Nashville, Tennessee 37235, United States;* orcid.org/0000-0001-5167-0731

Zili Wu − *Chemical Sciences Division, Oak Ridge National Laboratory, Oak Ridge, Tennessee 37831, United States; Center for Nanophase Materials Sciences, Oak Ridge National Laboratory, Oak Ridge, Tennessee 37831, United States;* orcid.org/0000-0002-4468-3240

Complete contact information is available at: https://pubs.acs.org/10.1021/acscatal.5c06321

Notes

The authors declare no competing financial interest.

ACKNOWLEDGMENTS

This research was supported by the U.S. Department of Energy, Office of Science, Office of Basic Energy Sciences, Chemical Sciences, Geosciences, and Biosciences Division, Catalysis Science program. The sample preparation, reaction test, and STEM studies were conducted as part of a user project at the Center for Nanophase Materials Sciences, which is a Department of Energy, Office of Science User Facility at Oak Ridge National Laboratory. Neutron scattering experiments were conducted at the VISION beamline at ORNL's Spallation Neutron Source, which is supported by the Scientific User Facilities Division, Office of Basic Energy Sciences (BES), U.S. Department of Energy (DOE), under Contract No. DE-AC0500OR22725 with UT-Battelle, LLC. XAS data were collected on the beamlines 4-3, 9-3, and 15-2 of the Stanford Synchrotron Radiation Lighthouse (SSRL), which is a U.S. Department of Energy Office of Science user facility at the SLAC National Laboratory, which is supported by the U.S. Department of Energy, Office of Science, Office of Basic Energy Sciences under Contract No. DE-AC02-76SF00515. The XAS experiments were performed by collaborating with Co-ACCESS, which is part of the SUNCAT Center for Interface Science and Catalysis and supported by the U.S. Department of Energy, Office of Basic Energy Sciences, Chemical Sciences, Geosciences and Biosciences Division. This manuscript has been authored by UT-Battelle, LLC under Contract No. DE-AC05-00OR22725 with the U.S. Department of Energy. The United States Government retains and the publisher, by accepting the article for publication, acknowledges that the United States Government retains a nonexclusive, paid-up, irrevocable, worldwide license to publish or reproduce the published form of this manuscript, or allow others to do so, for United States Government purposes. The Department of Energy will provide public access to these results of federally sponsored research in accordance with the DOE Public Access Plan (http://energy.gov/downloads/doe-public-access-plan).

REFERENCES

(1) Jiang, X.; Nie, X.; Guo, X.; Song, C.; Chen, J. G. Recent Advances in Carbon Dioxide Hydrogenation to Methanol via Heterogeneous Catalysis. *Chem. Rev.* **2020**, *120* (15), 7984−8034.

(2) Kanuri, S.; Roy, S.; Chakraborty, C.; Datta, S. P.; Singh, S. A.; Dinda, S. An insight of CO_2 hydrogenation to methanol synthesis: Thermodynamics, catalysts, operating parameters, and reaction mechanism. *Int. J. Energy Res.* **2022**, *46* (5), 5503−5522.

(3) Kattel, S.; Ramírez, P. J.; Chen, J. G.; Rodriguez, J. A.; Liu, P. Active sites for CO2 hydrogenation to methanol on Cu/ZnO catalysts. *Science* **2017**, *355* (6331), 1296−1299.

(4) Zabilskiy, M.; Sushkevich, V. L.; Palagin, D.; Newton, M. A.; Krumeich, F.; van Bokhoven, J. A. The unique interplay between copper and zinc during catalytic carbon dioxide hydrogenation to methanol. *Nat. Commun.* **2020**, *11* (1), No. 2409.

(5) Liang, H.; Zhang, G.; Li, Z.; Zhang, Y.; Fu, P. Catalytic hydrogenation of CO2 to methanol over Cu-based catalysts: Active sites profiling and regulation strategy as well as reaction pathway exploration. *Fuel Process. Technol.* **2023**, *252*, No. 107995.

(6) Kandemir, T.; Girgsdies, F.; Hansen, T. C.; Liss, K.-D.; Kasatkin, I.; Kunkes, E. L.; Wowsnick, G.; Jacobsen, N.; Schlögl, R.; Behrens, M. In Situ Study of Catalytic Processes: Neutron Diffraction of a Methanol Synthesis Catalyst at Industrially Relevant Pressure. *Angew. Chem., Int. Ed.* **2013**, *52* (19), 5166−5170.
(7) Li, K.; Chen, J. G. CO2 Hydrogenation to Methanol over ZrO2-Containing Catalysts: Insights into ZrO2 Induced Synergy. *ACS Catal.* **2019**, *9* (9), 7840−7861.
(8) Graciani, J.; Mudiyanselage, K.; Xu, F.; Baber, A. E.; Evans, J.; Senanayake, S. D.; Stacchiola, D. J.; Liu, P.; Hrbek, J.; Sanz, J. F.; Rodriguez, J. A. Highly active copper-ceria and copper-ceria-titania catalysts for methanol synthesis from CO_2. *Science* **2014**, *345* (6196), 546−550.
(9) Senanayake, S. D.; Ramírez, P. J.; Waluyo, I.; Kundu, S.; Mudiyanselage, K.; Liu, Z.; Liu, Z.; Axnanda, S.; Stacchiola, D. J.; Evans, J.; Rodriguez, J. A. Hydrogenation of CO_2 to Methanol on CeOx/Cu(111) and ZnO/Cu(111) Catalysts: Role of the Metal−Oxide Interface and Importance of Ce^{3+} Sites. *J. Phys. Chem. C* **2016**, *120* (3), 1778−1784.
(10) Wang, Y.; Kattel, S.; Gao, W.; Li, K.; Liu, P.; Chen, J. G.; Wang, H. Exploring the ternary interactions in Cu−ZnO−ZrO_2 catalysts for efficient CO_2 hydrogenation to methanol. *Nat. Commun.* **2019**, *10* (1), No. 1166.
(11) Wu, C.; Lin, L.; Liu, J.; Zhang, J.; Zhang, F.; Zhou, T.; Rui, N.; Yao, S.; Deng, Y.; Yang, F.; et al. Inverse ZrO_2/Cu as a highly efficient methanol synthesis catalyst from CO_2 hydrogenation. *Nat. Commun.* **2020**, *11* (1), No. 5767.
(12) Zhu, Y.; Zheng, J.; Ye, J.; Cui, Y.; Koh, K.; Kovarik, L.; Camaioni, D. M.; Fulton, J. L.; Truhlar, D. G.; Neurock, M.; et al. Copper-zirconia interfaces in UiO-66 enable selective catalytic hydrogenation of CO_2 to methanol. *Nat. Commun.* **2020**, *11* (1), No. 5849.
(13) Amann, P.; Klötzer, B.; Degerman, D.; Köpfle, N.; Götsch, T.; Lömker, P.; Rameshan, C.; Ploner, K.; Bikaljevic, D.; Wang, H.-Y.; et al. The state of zinc in methanol synthesis over a Zn/ZnO/Cu(211) model catalyst. *Science* **2022**, *376* (6593), 603−608.
(14) He, Y.; Li, Y.; Lei, M.; Polo-Garzon, F.; Perez-Aguilar, J.; Bare, S. R.; Formo, E.; Kim, H.; Daemen, L.; Cheng, Y.; et al. Significant Roles of Surface Hydrides in Enhancing the Performance of Cu/$BaTiO_{2.8}H_{0.2}$ Catalyst for CO_2 Hydrogenation to Methanol. *Angew. Chem., Int. Ed.* **2024**, *63* (1), No. e202313389.
(15) Li, Y.; Wu, Z. A review of in situ/operando studies of heterogeneous catalytic hydrogenation of CO_2 to methanol. *Catal. Today* **2023**, *420*, No. 114029.
(16) Fehr, S. M.; Krossing, I. Spectroscopic Signatures of Pressurized Carbon Dioxide in Diffuse Reflectance Infrared Spectroscopy of Heterogeneous Catalysts. *ChemCatChem* **2020**, *12* (9), 2622−2629.
(17) Divins, N. J.; Kordus, D.; Timoshenko, J.; Sinev, I.; Zegkinoglou, I.; Bergmann, A.; Chee, S. W.; Widrinna, S.; Karslıoğlu, O.; Mistry, H.; et al. Operando high-pressure investigation of size-controlled CuZn catalysts for the methanol synthesis reaction. *Nat. Commun.* **2021**, *12* (1), No. 1435.
(18) Tsoukalou, A.; Abdala, P. M.; Stoian, D.; Huang, X.; Willinger, M.-G.; Fedorov, A.; Müller, C. R. Structural Evolution and Dynamics of an In_2O_3 Catalyst for CO_2 Hydrogenation to Methanol: An Operando XAS-XRD and In Situ TEM Study. *J. Am. Chem. Soc.* **2019**, *141* (34), 13497−13505.
(19) Tsoukalou, A.; Abdala, P. M.; Armutlulu, A.; Willinger, E.; Fedorov, A.; Müller, C. R. Operando X-ray Absorption Spectroscopy Identifies a Monoclinic ZrO_2:In Solid Solution as the Active Phase for the Hydrogenation of CO_2 to Methanol. *ACS Catal.* **2020**, *10* (17), 10060−10067.
(20) Zabilskiy, M.; Sushkevich, V. L.; Newton, M. A.; Krumeich, F.; Nachtegaal, M.; van Bokhoven, J. A. Mechanistic Study of Carbon Dioxide Hydrogenation over Pd/ZnO-Based Catalysts: The Role of Palladium−Zinc Alloy in Selective Methanol Synthesis. *Angew. Chem., Int. Ed.* **2021**, *60* (31), 17053−17059.
(21) Zhang, F.; Liu, Z.; Chen, X.; Rui, N.; Betancourt, L. E.; Lin, L.; Xu, W.; Sun, C.-j.; Abeykoon, A. M. M.; Rodriguez, J. A.; et al. Effects of Zr Doping into Ceria for the Dry Reforming of Methane over Ni/$CeZrO_2$ Catalysts: In Situ Studies with XRD, XAFS, and AP-XPS. *ACS Catal.* **2020**, *10* (5), 3274−3284.
(22) Palomino, R. M.; Hamlyn, R.; Liu, Z.; Grinter, D. C.; Waluyo, I.; Rodriguez, J. A.; Senanayake, S. D. Interfaces in heterogeneous catalytic reactions: Ambient pressure XPS as a tool to unravel surface chemistry. *J. Electron Spectrosc. Relat. Phenom.* **2017**, *221*, 28−43.
(23) Seeger, P. A.; Daemen, L. L.; Larese, J. Z. Resolution of VISION, a crystal-analyzer spectrometer. *Nucl. Instrum. Methods Phys. Res., Sect. A* **2009**, *604* (3), 719−728.
(24) Hoffman, A. S.; Singh, J. A.; Bent, S. F.; Bare, S. R.; et al. In situ observation of phase changes of a silica-supported cobalt catalyst for the Fischer−Tropsch process by the development of a synchrotron-compatible in situ/operando powder X-ray diffraction cell. *J. Synchrotron Radiat.* **2018**, *25* (6), 1673−1682.
(25) Kresse, G.; Furthmüller, J. Efficiency of ab-initio total energy calculations for metals and semiconductors using a plane-wave basis set. *Comput. Mater. Sci.* **1996**, *6* (1), 15−50.
(26) Kresse, G.; Furthmüller, J. Efficient iterative schemes for ab initio total-energy calculations using a plane-wave basis set. *Phys. Rev. B* **1996**, *54* (16), No. 11169.
(27) Perdew, J. P.; Burke, K.; Ernzerhof, M. Generalized Gradient Approximation Made Simple. *Phys. Rev. Lett.* **1996**, *77* (18), No. 3865.
(28) Blöchl, P. E. Projector augmented-wave method. *Phys. Rev. B* **1994**, *50* (24), No. 17953.
(29) Kresse, G.; Joubert, D. From ultrasoft pseudopotentials to the projector augmented-wave method. *Phys. Rev. B* **1999**, *59* (3), No. 1758.
(30) Dion, M.; Rydberg, H.; Schröder, E.; Langreth, D. C.; Lundqvist, B. I. Van der Waals Density Functional for General Geometries. *Phys. Rev. Lett.* **2004**, *92* (24), No. 246401.
(31) K G, L.; Kundappaden, I.; Chatanathodi, R. A DFT study of CO adsorption on pt (111) using van der Waals functionals. *Surf. Sci.* **2019**, *681*, 143−148.
(32) Li, Y.; Wang, H.; Song, H.; Rui, N.; Kottwitz, M.; Senanayake, S. D.; Nuzzo, R. G.; Wu, Z.; Jiang, D.-e.; Frenkel, A. I. Active sites of atomically dispersed Pt supported on Gd-doped ceria with improved low temperature performance for CO oxidation. *Chem. Sci.* **2023**, *14* (44), 12582−12588.
(33) Ban, T.; Yu, X.-Y.; Kang, H.-Z.; Huang, Z.-Q.; Li, J.; Chang, C.-R. Design of SA-FLP Dual Active Sites for Nonoxidative Coupling of Methane. *ACS Catal.* **2023**, *13* (2), 1299−1309.
(34) Yang, W.; Song, H.; Zhang, L.; Zhang, J.; Polo-Garzon, F.; Wang, H.; Meyer, H., III; Jiang, D.-e.; Wu, Z.; Li, Y. Active Palladium Structures on Ceria Obtained by Tuning Pd−Pd Distance for Efficient Methane Combustion. *ACS Catal.* **2024**, *14* (21), 16459−16468.
(35) Li, Y.; Frenkel, A. I. Metal Nanocatalysts. In *XAFS Techniques for Catalysts, Nanomaterials, and Surfaces*; Iwasawa, Y.; Asakura, K.; Tada, M., Eds.; Springer International Publishing, 2017; pp 273−298.
(36) Phokha, S.; Swatsitang, E.; Maensiri, S. Room-temperature ferromagnetism in pure CeO_2 nanoparticles prepared by a simple direct thermal decomposition. *Electron. Mater. Lett.* **2015**, *11* (6), 1012−1020.
(37) Booth, C. H.; Walter, M. D.; Daniel, M.; Lukens, W. W.; Andersen, R. A. Self-Contained Kondo Effect in Single Molecules. *Phys. Rev. Lett.* **2005**, *95* (26), No. 267202.
(38) Wu, T.-S.; Syu, L.-Y.; Lin, B.-H.; Weng, S.-C.; Jeng, H.-T.; Huang, Y.-S.; Soo, Y.-L. Reduction of dopant ions and enhancement of magnetic properties by UV irradiation in Ce-doped TiO_2. *Sci. Rep.* **2021**, *11* (1), No. 7668.
(39) Wu, Z.; Cheng, Y.; Tao, F.; Daemen, L.; Foo, G. S.; Nguyen, L.; Zhang, X.; Beste, A.; Ramirez-Cuesta, A. J. Direct Neutron Spectroscopy Observation of Cerium Hydride Species on a Cerium Oxide Catalyst. *J. Am. Chem. Soc.* **2017**, *139* (28), 9721−9727.
(40) Li, Y.; Kottwitz, M.; Vincent, J. L.; Enright, M. J.; Liu, Z.; Zhang, L.; Huang, J.; Senanayake, S. D.; Yang, W.-C. D.; Crozier, P. A.; et al. Dynamic structure of active sites in ceria-supported Pt

https://doi.org/10.1021/acscatal.5c06321
ACS Catal. 2026, 16, 1132−1143

catalysts for the water gas shift reaction. *Nat. Commun.* **2021**, *12* (1), No. 914.
(41) Günter, T.; Carvalho, H. W. P.; Doronkin, D. E.; Sheppard, T.; Glatzel, P.; Atkins, A. J.; Rudolph, J.; Jacob, C. R.; Casapu, M.; Grunwaldt, J.-D. Structural snapshots of the SCR reaction mechanism on Cu-SSZ-13. *Chem. Commun.* **2015**, *51* (44), 9227−9230.
(42) Li, Y.; Kraynis, O.; Kas, J.; Weng, T.-C.; Sokaras, D.; Zacharowicz, R.; Lubomirsky, I.; Frenkel, A. I. Geometry of electromechanically active structures in Gadolinium - doped Cerium oxides. *AIP Adv.* **2016**, *6* (5), No. 055320, DOI: 10.1063/1.4952645.
(43) Elsen, A.; Jung, U.; Vila, F.; Li, Y.; Safonova, O. V.; Thomas, R.; Tromp, M.; Rehr, J. J.; Nuzzo, R. G.; Frenkel, A. I. Intracluster Atomic and Electronic Structural Heterogeneities in Supported Nanoscale Metal Catalysts. *J. Phys. Chem. C* **2015**, *119* (45), 25615−25627.
(44) Hämäläinen, K.; Siddons, D. P.; Hastings, J. B.; Berman, L. E. Elimination of the inner-shell lifetime broadening in x-ray-absorption spectroscopy. *Phys. Rev. Lett.* **1991**, *67* (20), No. 2850.
(45) Safonova, O. V.; Tromp, M.; van Bokhoven, J. A.; de Groot, F. M. F.; Evans, J.; Glatzel, P. Identification of CO Adsorption Sites in Supported Pt Catalysts Using High-Energy-Resolution Fluorescence Detection X-ray Spectroscopy. *J. Phys. Chem. B* **2006**, *110* (33), 16162−16164.
(46) van Bokhoven, J. A.; Louis, C.; Miller, J. T.; Tromp, M.; Safonova, O. V.; Glatzel, P. Activation of Oxygen on Gold/Alumina Catalysts: In Situ High-Energy-Resolution Fluorescence and Time-Resolved X-ray Spectroscopy. *Angew. Chem., Int. Ed.* **2006**, *45* (28), 4651−4654.
(47) de Groot, F. M. F.; Krisch, M. H.; Vogel, J. Spectral sharpening of the Pt L edges by high-resolution x-ray emission. *Phys. Rev. B* **2002**, *66* (19), No. 195112.
(48) Zhang, F.; Wang, P.; Koberstein, J.; Khalid, S.; Chan, S.-W. Cerium oxidation state in ceria nanoparticles studied with X-ray photoelectron spectroscopy and absorption near edge spectroscopy. *Surf. Sci.* **2004**, *563* (1), 74−82.
(49) Korobko, R.; Patlolla, A.; Kossoy, A.; Wachtel, E.; Tuller, H. L.; Frenkel, A. I.; Lubomirsky, I. Giant Electrostriction in Gd-Doped Ceria. *Adv. Mater.* **2012**, *24* (43), 5857−5861.
(50) Korobko, R.; Lerner, A.; Li, Y.; Wachtel, E.; Frenkel, A. I.; Lubomirsky, I. In-situ extended X-ray absorption fine structure study of electrostriction in Gd doped ceria. *Appl. Phys. Lett.* **2015**, *106* (4), No. 042904, DOI: 10.1063/1.4906857.
(51) Roiaz, M.; Falivene, L.; Rameshan, C.; Cavallo, L.; Kozlov, S. M.; Rupprechter, G. Roughening of Copper (100) at Elevated CO Pressure: Cu Adatom and Cluster Formation Enable CO Dissociation. *J. Phys. Chem. C* **2019**, *123* (13), 8112−8121.
(52) Gunathunge, C. M.; Li, J.; Li, X.; Waegele, M. M. Surface-Adsorbed CO as an Infrared Probe of Electrocatalytic Interfaces. *ACS Catal.* **2020**, *10* (20), 11700−11711.
(53) Topsøe, N.-Y.; Topsøe, H. FTIR studies of dynamic surface structural changes in Cu-based methanol synthesis catalysts1Received 4 December 1997; accepted 20 March 1998.1. *J. Mol. Catal. A: Chem.* **1999**, *141* (1), 95−105.
(54) Zhang, Y.; Chen, Y.; Wang, X.; Feng, Y.; Dai, Z.; Cheng, M.; Zhang, G. Low-coordinated copper facilitates the *CH2CO affinity at enhanced rectifying interface of Cu/Cu2O for efficient CO2-to-multicarbon alcohols conversion. *Nat. Commun.* **2024**, *15* (1), No. 5172.
(55) Wan, Q.; Wei, F.; Wang, Y.; Wang, F.; Zhou, L.; Lin, S.; Xie, D.; Guo, H. Single atom detachment from Cu clusters, and diffusion and trapping on CeO2(111): implications in Ostwald ripening and atomic redispersion. *Nanoscale* **2018**, *10* (37), 17893−17901.
(56) Fritsch, L.; Rehsies, P.; Barakat, W.; Estes, D. P.; Bauer, M. Detection and Characterization of Hydride Ligands in Copper Complexes by Hard X-Ray Spectroscopy. *Chem. - Eur. J.* **2024**, *30* (36), No. e202400357.
(57) Edwards, A. J.; Dhayal, R. S.; Liao, P.-K.; Liao, J.-H.; Chiang, M.-H.; Piltz, R. O.; Kahlal, S.; Saillard, J.-Y.; Liu, C. W. Chinese Puzzle Molecule: A 15 Hydride, 28 Copper Atom Nanoball. *Angew. Chem., Int. Ed.* **2014**, *53* (28), 7214−7218.
(58) Vayssilov, G. N.; Mihaylov, M.; Petkov, P. S.; Hadjiivanov, K. I.; Neyman, K. M. Reassignment of the Vibrational Spectra of Carbonates, Formates, and Related Surface Species on Ceria: A Combined Density Functional and Infrared Spectroscopy Investigation. *J. Phys. Chem. C* **2011**, *115* (47), 23435−23454.
(59) Fehr, S. M.; Nguyen, K.; Krossing, I. Realistic Operando-DRIFTS Studies on Cu/ZnO Catalysts for CO_2 Hydrogenation to Methanol − Direct Observation of Mono-ionized Defect Sites and Implications for Reaction Intermediates. *ChemCatChem* **2022**, *14* (3), No. e202101500.
(60) Lustemberg, P. G.; Bosco, M. V.; Bonivardi, A.; Busnengo, H. F.; Ganduglia-Pirovano, M. V. Insights into the Nature of Formate Species in the Decomposition and Reaction of Methanol over Cerium Oxide Surfaces: A Combined Infrared Spectroscopy and Density Functional Theory Study. *J. Phys. Chem. C* **2015**, *119* (37), 21452−21464.
(61) Sugiyama, H.; Miyazaki, M.; Sasase, M.; Kitano, M.; Hosono, H. Room-Temperature CO_2 Hydrogenation to Methanol over Air-Stable hcp-PdMo Intermetallic Catalyst. *J. Am. Chem. Soc.* **2023**, *145* (17), 9410−9416.
(62) Hu, J.; Yu, L.; Deng, J.; Wang, Y.; Cheng, K.; Ma, C.; Zhang, Q.; Wen, W.; Yu, S.; Pan, Y.; et al. Sulfur vacancy-rich MoS_2 as a catalyst for the hydrogenation of CO_2 to methanol. *Nat. Catal.* **2021**, *4* (3), 242−250.
(63) Uvdal, P.; Weldon, M. K.; Friend, C. M. Adsorbate symmetry and Fermi resonances of methoxide adsorbed on Mo(110) as studied by surface infrared spectroscopy. *Phys. Rev. B* **1994**, *50* (16), No. 12258.
(64) Ojelade, O. A.; Zaman, S. F. A Review on Pd Based Catalysts for CO_2 Hydrogenation to Methanol: In-Depth Activity and DRIFTS Mechanistic Study. *Catal. Surv. Asia* **2020**, *24* (1), 11−37.
(65) Badri, A.; Binet, C.; Lavalley, J.-C. Use of methanol as an IR molecular probe to study the surface of polycrystalline ceria. *J. Chem. Soc., Faraday Trans.* **1997**, *93* (6), 1159−1168.
(66) Wang, W.; Qu, Z.; Song, L.; Fu, Q. CO_2 hydrogenation to methanol over Cu/CeO_2 and Cu/ZrO_2 catalysts: Tuning methanol selectivity via metal-support interaction. *J. Energy Chem.* **2020**, *40*, 22−30.
(67) Vergara, T.; Gómez, D.; de Oliveira Campos, B. L.; Delgado, K. H.; Jiménez, R.; Karelovic, A. Disclosing the Reaction Mechanism of CO2 Hydrogenation to Methanol over CuCeOx/TiO2: A Combined Kinetic, Spectroscopic, and Isotopic Study. *ACS Catal.* **2023**, *13* (22), 14699−14715.
(68) Zhu, J.; Su, Y.; Chai, J.; Muravev, V.; Kosinov, N.; Hensen, E. J. M. Mechanism and Nature of Active Sites for Methanol Synthesis from CO/CO2 on Cu/CeO2. *ACS Catal.* **2020**, *10* (19), 11532−11544.

https://doi.org/10.1021/acscatal.5c06321
ACS Catal. 2026, 16, 1132−1143